Development and modeling of a polar-direct-drive exploding pusher platform at the National Ignition Facility

C. Leland Ellison, Heather D. Whitley, Colin R. D. Brown, Sean R. Copeland, Warren J. Garbett, Hai P. Le, Marilyn B. Schneider, Zachary B. Walters, Hui Chen, John I. Castor, R. Stephen Craxton, Maria Gatu Johnson, Emma M. Garcia, Frank R. Graziani, G. Elijah Kemp, Christine M. Krauland, Patrick W. McKenty, Brandon Lahmann, Jesse E. Pino, Michael S. Rubery, Howard A. Scott, Ronnie Shepherd, and Hong Sio

Citation: Physics of Plasmas **25**, 072710 (2018); doi: 10.1063/1.5025724
View online: https://doi.org/10.1063/1.5025724
View Table of Contents: http://aip.scitation.org/toc/php/25/7
Published by the American Institute of Physics

Development and modeling of a polar-direct-drive exploding pusher platform at the National Ignition Facility

C. Leland Ellison,[1,a)] Heather D. Whitley,[1] Colin R. D. Brown,[2] Sean R. Copeland,[1] Warren J. Garbett,[2] Hai P. Le,[1] Marilyn B. Schneider,[1] Zachary B. Walters,[1] Hui Chen,[1] John I. Castor,[1] R. Stephen Craxton,[3] Maria Gatu Johnson,[4] Emma M. Garcia,[3] Frank R. Graziani,[1] G. Elijah Kemp,[1] Christine M. Krauland,[5] Patrick W. McKenty,[3] Brandon Lahmann,[4] Jesse E. Pino,[1] Michael S. Rubery,[2] Howard A. Scott,[1] Ronnie Shepherd,[1] and Hong Sio[4]

[1]*Lawrence Livermore National Laboratory, Livermore, California 94550, USA*
[2]*AWE plc, Aldermaston, Reading, Berkshire, RG7 4PR, United Kingdom*
[3]*Laboratory for Laser Energetics, University of Rochester, Rochester, New York 14636, USA*
[4]*Massachusetts Institute of Technology, Cambridge, Massachusetts 02139, USA*
[5]*General Atomics, San Diego, California 92186, USA*

(Received 12 February 2018; accepted 5 July 2018; published online 30 July 2018)

High-intensity laser facilities, such as the National Ignition Facility (NIF), enable the experimental investigation of plasmas under extreme, high-energy-density conditions. Motivated by validating models for collisional heat-transfer processes in high-energy-density plasmas, we have developed an exploding pusher platform for use at the NIF in the polar-direct-drive configuration. The baseline design employs a 3 mm-diameter capsule, an 18 μm-thick CH ablator, and Ar-doped D_2 gas to achieve several keV electron-ion temperature separations with relatively low convergence ratios. In an initial series of shots at the NIF—N160920–003, -005, and N160921–001—the ratio of the laser intensity at different polar angles was varied to optimize the symmetry of the implosion. Here we summarize experimental results from the shot series and present pre- and post-shot analysis. Although the polar-direct-drive configuration is inherently asymmetric, we successfully tuned a post-shot 1D model to a set of key implosion performance metrics. The post-shot model has proven effective for extrapolating capsule performance to higher incident laser drive. Overall, the simplicity of the platform and the efficacy of the post-shot 1D model make the polar-direct-drive exploding pusher platform attractive for a variety of applications beyond the originally targeted study of collisional processes in high-energy-density plasmas. *Published by AIP Publishing.*
https://doi.org/10.1063/1.5025724

I. INTRODUCTION

The National Ignition Facility (NIF) enables the study of matter over unprecedented regimes of temperature and density.[1] While the ultimate goal is to achieve ignition for inertial confinement fusion (ICF),[2,3] an associated goal is the testing and validation of integrated physics codes designed to simulate the physical processes occurring under these regimes. Many of the experiments at the NIF employ a hohlraum-based indirect-drive configuration; however, several recent experiments have adapted the existing laser configuration to achieve "polar-direct-drive" (PDD) for hohlraum-free implosions.[4–12] Although the symmetry is not ideal for ignition-relevant, high-convergence-ratio platforms, PDD allows the fielding of lower-convergence-ratio direct-drive platforms, including exploding pushers,[13–16] without re-configuring the beamlines. These platforms are suitable for validating integrated simulation capabilities en route to ignition.

In this paper, we describe capsule design considerations, initial experimental results, and 1D post-shot modeling of a new polar-direct-drive exploding pusher (PDXP) platform fielded at the NIF in September 2016, specifically during shot numbers N160920-003, N160920-005, and N160921-001 (NIF shot numbers are in the format Nyymmdd-xxx, where yy is the year of the shot, mm the month, dd the date, and xxx a daily shot identifier.) This PDXP platform was originally designed to provide validation data for fundamental heat transport models and, in particular, to measure the electron-ion equilibration rate, which was examined in detail by Benedict *et al.*[17] for a weakly coupled hydrogen plasma. More recently, the platform has been utilized for nucleosynthesis experiments[18] and diagnostic qualification shots,[19,20] and to produce high neutron yields.[21,22] We use a 3 mm-diameter capsule comprising an 18 μm-thick glow-discharge polymer (GDP) shell filled with 8 atm of D_2 gas. The proposed thermal transport measurements would utilize time-resolved measurements of spectroscopic signals created by small amounts of Ar gas added as a dopant to diagnose the plasma conditions as a function of time. The electron temperature can be deduced from the line ratio of the Ar K-shell emission (Ly-α/He-α), while the electron density can be determined through examining Stark broadening in the Ly-γ lines. This platform is potentially advantageous for these types of measurements since (1) eliminating the hohlraum enables better diagnostic access to the capsule, (2) the direct drive provides a means of driving stronger shocks to more

a)Author to whom correspondence should be addressed: ellison6@llnl.gov

effectively obtain higher ion temperatures and larger electron-ion temperature differences, and (3) the capsules are easy to fabricate using existing capabilities.[23]

One desirable goal to make the platform useful for studying thermal transport is that the capsule dynamics should ultimately be described well using 1D models. Extracting data about electron-ion coupling and/or thermal conductivity will be complicated, and perhaps impossible, if the geometry of the inner gas region is dominated by 2D or 3D features that lead to significant perturbation of the gas conditions due to mix or other processes. To meet the goal of achieving an essentially 1D implosion, our September 2016 PDXP shots were aimed at providing data to assist in tuning the PDXP laser configuration to minimize 2D and 3D effects. In the three shots, the spatial distribution of the laser intensity on the target surface was varied by adjusting the relative intensity of the inner (23.5° and 30°) beams, incident near the capsule poles, compared with the outer (44.5° and 50°) beams, incident near the equator, while the pointing of the laser beams and the total energy delivered by the laser were nominally held constant. In these shots, we demonstrated that changing the relative intensity of the drive between the inner and outer beams is a viable means for changing the symmetry of the implosion of these capsules. Those results are shown briefly here and discussed in more detail in a forthcoming publication.[24]

The focus of this paper is to determine the capabilities and limitations of 1D radiation-hydrodynamics simulations for describing the three PDXP shots. Specifically, we present pre-shot design calculations and post-shot model adjustments using the Ares[25,26] and Nym[27] codes. We motivate the nominal design parameters by showing diagnosable electron-ion temperature separation in the pre-shot calculations. Perhaps unsurprisingly, the 1D pre-shot calculations overestimate the neutron yield and peak ion temperatures relative to the experiments, while underestimating the bang time. To compensate during post-shot modeling, we employ an ensemble sampling approach to scan variations in typical model parameters, including the laser energy multiplier, the electron thermal flux limiter,[28,29] and a diffusive mix parameter. We then quantify how well each computed model fits various data obtained in the September 2016 shots. We find that, with appropriate choices of these parameters, it is possible to closely match the measured X-ray bang times, DD neutron yields, and reaction-weighted ion temperatures. Although 2D simulations are required to capture the shape of the implosion (the subject of a forthcoming publication[24]), we demonstrate the efficacy of the 1D post-shot model by successfully predicting the dependence of bang time on laser energy observed in a later sequence of NIF shots.[18]

II. DESIGN OF THE NOMINAL PLATFORM

A. Modeling tools

One of the most heavily used codes for this work was Lawrence Livermore National Laboratory's Ares multi-physics radiation hydrodynamics code. Ares solves the single-fluid-velocity, multi-material, multi-component Navier-Stokes equations using a staggered-mesh arbitrary Lagrangian-Eulerian (ALE) predictor-corrector scheme. In these 1D studies, the mesh was evolved in a purely Lagrangian mode. Although the multiple constituent ion species are treated as a single fluid, separate ion, electron, and radiation temperatures are evolved in time. The electron and ion temperatures collisionally equilibrate according to a rate derived by Brysk[30] or a higher-fidelity (Coulomb-log-free) rate recently derived by Scullard *et al.*[31] using a quantum Lenard-Balescu treatment. During the evolution of the electron temperature, the thermal diffusion is limited by a user-specified flux limiter,[28,29] which is important for the high-temperature-gradient regimes experienced by directly driven capsules.[15,29] The radiation temperature is evolved in the radiation-diffusion approximation, and local thermodynamic equilibrium (LTE) is assumed. Although proper treatment of the Ar dopant should include non-LTE effects, simulations demonstrate that the small atomic fraction of Ar does not affect the hydrodynamics and the spectroscopic information can be post-processed using the Cretin atomic kinetics code[32] (which includes non-LTE effects). Laser energy is propagated into the simulation along radially incident rays and deposited according to the inverse bremsstrahlung mechanism. When a laser ray reaches the critical surface, the remainder of the laser energy is deposited. Because this model tends to overestimate the amount of energy absorbed by the capsule, a laser energy multiplier is used during modeling. Other codes employing non-radially incident laser rays (Nym, SAGE[33]) absorbed approximately 80% of the laser energy.

Noteworthy limitations of the Ares code for modeling this platform include the absence of laser-plasma interaction (LPI) models and the lack of a non-local electron transport model, both believed to be important for polar-direct-drive platforms at the NIF,[9] although the extent to which they impact the simpler PDXP platform forms part of ongoing assessments of our data set.

We also modeled the new platform with Nym. Nym is a Lagrangian single-fluid code with separate ion, electron, and radiation temperatures and similar energy coupling physics and flux-limited thermal conduction. The 1D simulations shown here use implicit Monte Carlo radiation transport. A key variation from the 1D Ares model is the laser energy propagation and deposition. Nym uses an axisymmetric 2D ray propagation scheme to include non-radially incident rays. Energy is deposited via inverse bremsstrahlung absorption, with additional user-defined deposition near critical density to approximate resonant processes. Based on previous experience at the Omega laser facility,[15] this fraction was set to 10% of the remaining ray energy.

B. Design considerations and nominal platform

In order to develop a platform that is calculable, diagnosable, and sensitive to collisional energy exchange processes, we performed sets of 1D radiation-hydrodynamic simulations scanning possible capsule and laser power configurations.

A suitable design needs to balance a number of top-level requirements: hydrodynamic stability, to avoid shell-gas mixing; low to moderate convergence, to reduce the impact of any drive asymmetry; sufficiently high temperatures

(>2.5 keV) and temperature separation persisting for sufficient duration (>200 ps) to enable spectroscopic diagnosis of temperature equilibration rates; and sensitivity to the relevant collisional processes.

Our choice of exploding pushers for this study was motivated by the previous work of Miles *et al.*,[14] where it was demonstrated that the strong shocks produced in exploding pushers could drive large separations in electron and ion temperatures. Meanwhile, we chose a direct drive because NIF experiments and Ares calculations indicated that the conditions in indirect-drive exploding pushers[16] would not allow the spectroscopic measurements we proposed. PDXP implosions potentially achieve much higher temperatures to meet spectroscopic requirements.

Plastic glow-discharge-polymer (GDP) capsules were chosen due to both target fabrication considerations and favorable behavior in our design studies. Acceptable performance was also found with Be and SiO_2 capsules; however, these materials were unfavorable for spectroscopy. For SiO_2, radiation-hydrodynamic simulations and Cretin calculations both showed that the X-ray background from the hot, ablated coronal plasma would obscure Ar spectroscopy. Beryllium was also eliminated as a candidate because the current fabrication process uses Ar, which unavoidably results in Ar inclusion within the Be matrix, disrupting interpretation of Ar spectroscopy of the compressed gas.

Optimization of the design space identified a number of competing trade-offs. A larger capsule diameter was found to be beneficial, providing increased yield, longer timescales, and reduced spatial gradients. However, target fabrication imposes a lower limit on the shell thickness for a given diameter, which in turn imposes a maximum limit on the gas fill pressure. Higher pressure is advantageous in reducing convergence, and therefore susceptibility to drive asymmetry, but also reduces the stagnation temperature. Consideration of the laser pulse, chosen as a simple square power profile, showed that the capsule dynamics generally become more impulsive (exploding pusher-like) at higher intensity, with no coasting phase, lower convergence, and higher temperature. An upper limit of 10^{15} W cm^{-2} was imposed on the intensity to reduce the risk of detrimental laser-plasma instabilities that could impact both energy coupling and symmetry. The selected baseline design was a 3 mm-diameter, 18 μm-thick GDP shell filled with 8 atm of D_2 gas and driven by a 1.75 ns FWHM, 478 kJ laser pulse. The capsule was supported by a 30 μm borosilicate fill tube with an approximately 100 μm diameter glue spot. See Fig. 1 for an illustration of the target.

One-dimensional Ares simulations without mix predicted that this platform would achieve a yield of 1.1×10^{14} DD neutrons while exhibiting diagnosable levels of electron-ion temperature separation. Figure 2 shows spatial and temporal histories of ion temperature, electron temperature, and mass density for the nominal pre-shot design. The color map in panel (a) shows the ion temperature as a function of radial position and time. Radial profiles of mass density, ion temperature, and electron temperature at different instances in time are shown in panels (b), (c), and (d), respectively. Design parameters were chosen to achieve small thermal and density gradients across a large volume of the gas. During a window of time of about 200 ps, between 2.3 ns and 2.5 ns, the temperature profiles for both ions and electrons meet our requirements. This window of time occurs between the initial shock heating and a recompression after the shock reflects from the gas-shell interface. As shown in the radial profiles, the temperatures and densities of the gas during this window are relatively constant within the inner radius of the gas.

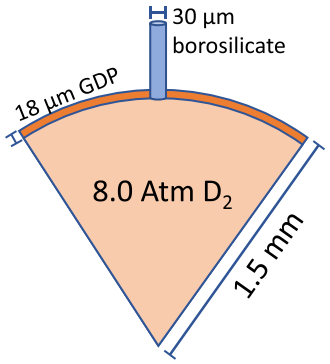

FIG. 1. Schematic of the PDXP target, which uses 8 atm of deuterium gas surrounded by an 18 μm-thick GDP shell and supported by a 30 μm borosilicate fill tube.

To determine the concentration of Ar dopant to be added to the deuterium gas, we post-processed output from the Ares runs with Cretin in order to find the minimum level necessary to produce a good signal-to-noise spectral signal. Additional Ares and Nym calculations were used to determine the maximum concentration of Ar that could be added to the deuterium gas without perturbing the implosion. Balancing these design objectives, we specified 0.004–0.005 atm of Ar dopant (received 0.0046 atm) in the 8 atm of D_2 gas.

III. SHAPING STUDIES

The nominal PDXP design was fielded at the NIF during shot numbers N160920-003, N160920-005, and N160921-001, henceforth referred to as "Shot 1," "Shot 2," and "Shot 3," respectively. This initial set of experiments was devoted to optimizing the symmetry of the implosion within the constraints of the polar-direct-drive configuration. For all shots, the same beam pointing was prescribed according to an optimization performed using the SAGE radiation-hydrodynamics code. The "laser cone fraction"—the ratio of the energy in the 23.5° and 30° beams to the total laser energy—was varied across the experiments, and was 33% for Shot 1, 28% for Shot 2, and 22% for Shot 3. Because there are twice as many outer beams as inner beams, Shot 1 represents equal power for each beam with a nominal on-target intensity of 1×10^{15} W/cm^2. All experiments utilized the nominal capsule design and the same (nominally) square-pulse laser drive with a total energy of 478 kJ. Laser and capsule parameters are provided in Table I. The delivered laser energy for Shot 3 was slightly lower than desired because two quads of laser beams were dropped for the shot (one for unanticipated circumstances and the opposite quad to preserve symmetry). Two-dimensional pre-shot modeling predicted that this range of laser cone fractions would yield implosions ranging from oblate (wide at the equator) to prolate (wide at the pole).

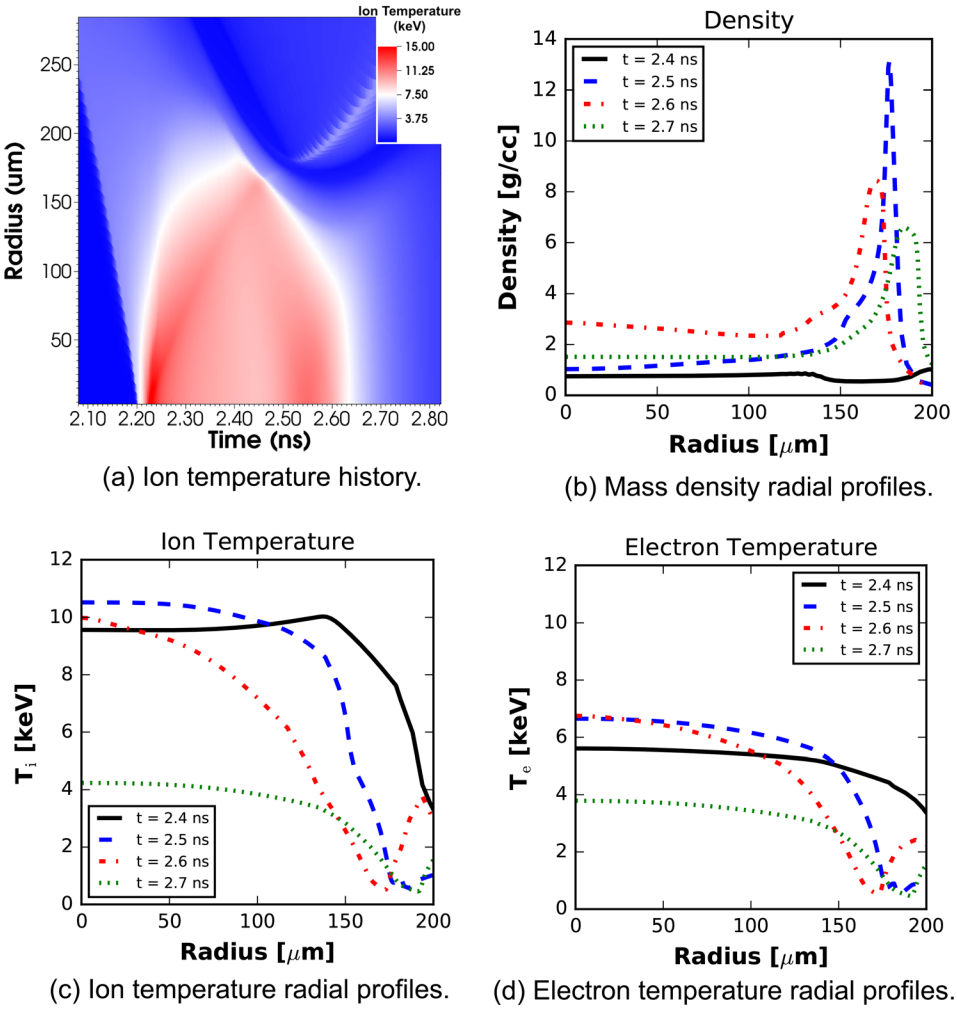

FIG. 2. Pre-shot modeling of the ion temperature history (a), and radial profiles of the mass density (b), ion temperature T_i (c), and electron temperature T_e (d) at four successive times near stagnation.

The PDXP shaping studies were supported by an array of diagnostics. To measure shape, gated X-ray diagnostics (GXDs) captured in-flight images of the capsule's X-ray emission. One GXD observed the implosion from the equator, while another captured images from the pole. The azimuthally symmetric illumination resulted in good polar symmetry, so the equatorial GXD images were of primary interest for characterizing the shape of the implosion. Both GXDs were configured to capture early-time images (up to 2 ns) where the symmetry may most directly be related to the laser drive. Spatially integrating X-ray diagnostics were also used, including a time-resolved X-ray streak camera (SPIDER),[34] a time-resolved soft X-ray detector (Dante),[35] a time-integrated spectrometer (VIRGIL),[36] and a time-resolved spectrometer (NXS).[37] SPIDER supplied the X-ray emission history, allowing the identification of the X-ray bang time (time of peak emission) and the X-ray burn width (full-width-half-max of the spatially and energy-integrated emission in four separately filtered channels). Dante supplemented this information with broad-band soft X-ray spectra. Meanwhile, the time-resolved and time-integrated spectrometers measured K-shell emission from the Ar dopant, which can be used to estimate electron temperature. Nuclear diagnostics included four neutron time-of-flight (nToF) detectors to measure primary (DD) and secondary (DT) neutron yields and to enable calculation of a "burn-averaged" ion temperature.[38] Finally, laser backscatter was diagnosed using the near backscatter imager (NBI) and full aperture backscatter (FABS) diagnostics.[39,40] The backscatter measurements indicated significant laser-plasma interactions, consistent with previous polar-direct-drive experiments.[9] The measurements also exhibited strong angular variation, requiring multi-dimensional modeling for comparisons.

TABLE I. Summary of the three shots discussed: laser cone fraction f_{cone}, total laser energy E_{laser}, outer capsule diameter d_{outer}, shell thickness Δr_{shell}, and fill pressure P_{D_2}.

	f_{cone}	E_{laser} (kJ)	d_{outer} (μm)	Δr_{shell} (μm)	P_{D_2} (atm)
Shot 1: N160920-003	0.33	473	2956	18.0	7.78
Shot 2: N160920-005	0.28	474	2955	19.0	7.94
Shot 3: N160921-001	0.22	459	2953	18.5	7.96

Scalar performance measurements for the three shots are presented in Table II. Shot 2 performed the best, with a DD neutron yield of 2.1×10^{13} and an nToF ion temperature of 7.8 keV. The X-ray bang times for the three shots were largely similar, all near 3.2 ns. These measurements indicate that the nominal pre-shot 1D modeling over-estimated the yield of the implosion; the X-ray bang time was predicted to be near 2.6 ns in the pre-shot Ares model, and the yield was predicted to be 1.1×10^{14} neutrons in clean simulations and

TABLE II. Scalar performance measurements for the three shots, including x-ray bang time $t_{\text{x–ray bang}}$, the full-width half-maximum of the x-ray production time $\text{FWHM}_{\text{x–ray}}$, DD neutron yield Y_{DDn}, DT neutron yield Y_{DTn}, and nToF ion temperature T_{ion}.

	$t_{\text{x–ray bang}}$ (ns)	$\text{FWHM}_{\text{x–ray}}$ (ns)	Y_{DDn} (10^{13})	Y_{DTn} (10^{9})	T_{ion} (keV)
Shot 1: N160920-003	3.28	0.54	1.61 ± 0.07	7.73 ± 0.4	7.66 ± 0.39
Shot 2: N160920-005	3.18	0.45	2.11 ± 0.10	10.4 ± 0.5	7.81 ± 0.39
Shot 3: N160921-001	3.16	0.38	1.83 ± 0.10	8.74 ± 0.44	7.32 ± 0.53

2.9×10^{13} using a "fall-line" model that truncates the yield after the shock reflection.[16] The simulated burn-averaged ion temperature reached 9 keV. In Sec. IV, we investigate the extent to which these discrepancies can be accounted for with a chosen set of parameters in a 1D model.

To assess the shape of the implosions, the equatorial GXD images were analyzed at each instant in time to extract the ratio of the capsule diameter at the pole to the diameter at the equator. Figure 3 shows a representative GXD image, acquired at 0.86 ns. Figure 4 shows the time evolution of the pole/equator ratio for the different shots. Shot 1 can be classified as the most oblate implosion, Shot 2 as slightly oblate, and Shot 3 as slightly prolate. A more detailed analysis of the shape, including Legendre mode decomposition and comparisons with 2D simulations, will be presented in Ref. 24.

IV. POST-SHOT MODELING

Equipped with the initial series of data, we sought to constrain uncertain parameters and partially compensate for missing physics in the 1-D Ares model—such as laser-plasma interactions and non-local electron transport—by adjusting model parameters to best match the experimental data. Although some of the missing physics (for example, multi-dimensional asymmetries) can never be fully accounted for within the available 1D model, adjusting simulation parameters is common practice to compensate for missing effects while establishing a more predictive model.[14,15] Such models are potentially useful for predicting the outcome of other experiments sufficiently nearby in the design parameter space. Ultimately, we were able to find good agreement with a representative subset of the measured results using three commonly varied model parameters. Because these parameters introduce substantial freedom in the numerical predictions, we advocate for the efficacy of this post-shot model by presenting a successful prediction of an experiment performed in the spring of 2017 that used the same target but with a different gas fill and increased laser power.[18] Finally, we reassess the electron and ion temperature separation histories using the post-shot model.

To constrain the post-shot model parameters, we chose a subset of the experimental measurements based on small uncertainty and directness of comparison to simulated quantities. In particular, we used the X-ray bang time, the DD neutron yield, and the neutron-averaged ion temperature as the main performance metrics for establishing the post-shot model. The X-ray bang time is the principal indicator of the amount of laser energy coupled into the capsule, enabling a choice of parameters that mimics the effects of uncertain energy coupling and loss mechanisms, including laser-plasma interactions. The neutron yield, although also influenced by the capsule drive, introduces dependence on the state of the fuel, allowing the adjustment of models accounting for mixing of the shell material into the gas. Finally, the nToF ion temperature, extracted from the measured neutron spectra, is comparable with simulated burn-averaged temperatures and serves as a time-integrated constraint for multiple relevant simulation parameters.

To compare nToF-inferred ion temperatures with burn-averaged simulation temperatures in Ares, a linear adjustment between the two quantities was calculated using Nym, which has a synthetic nToF capability. The nToF and burn-averaged temperatures can differ due to broadening of the measured neutron spectrum by bulk hydrodynamic motion.[41,42] To

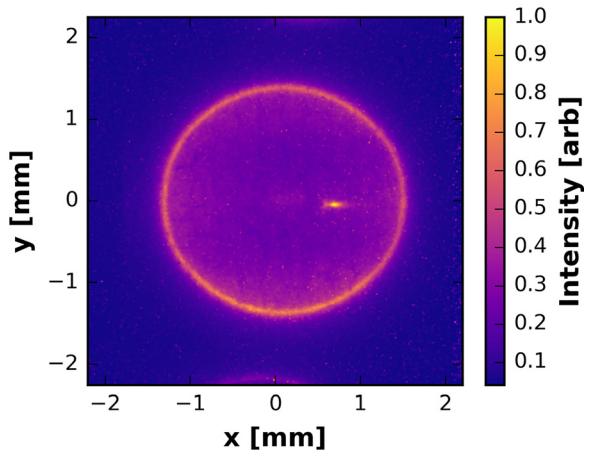

FIG. 3. Equatorial GXD image taken from Shot 2 at 0.86 ns. The fill tube imparts a bright spot on the right side of the image.

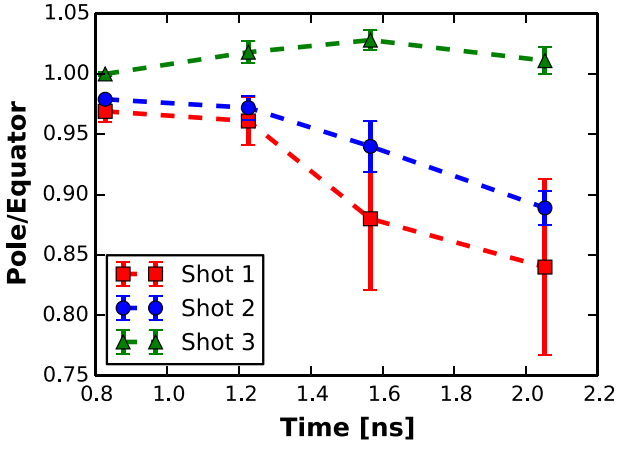

FIG. 4. Time evolution of the ratio of the capsule diameter at the pole to that at the equator, indicating that the implosion shape ranged from oblate to prolate from Shot 1 to Shot 3. Each marker depicts the average pole-to-equator ratio of between 2 and 4 GXD images taken near similar times. The error bars indicate the maximum and minimum ratio for each set of images.

assess this effect, 1D Nym simulations were performed with a variety of energy multipliers and flux limiters. The two temperatures were found to be related by a predominately linear trend, as shown in Fig. 5. When comparing simulated burn-averaged temperatures to experimental nToF temperatures, we applied a linear correction based on a least squares fit to the dataset in Fig. 5. In the regime of interest, the linear correction adds about 0.5 keV to the simulated burn-averaged ion temperature.

To match the experimental data, three model parameters were chosen based on a combination of their large uncertainty, significant influence on the results, and relevance to known shortcomings of the model. These fit parameters are: an "energy multiplier" that scales the incident laser intensity, an "electron heat flux limiter" that restricts the maximum electron thermal flux,[28,29] and a "diffusion multiplier" that scales the rate of atomic diffusion. The energy multiplier is intended to account for drive-reducing mechanisms, including plasma-induced laser scattering. The electron (thermal) flux limiter is commonly used to compensate for limitations of the diffusion approximation to heat flow in the presence of strong thermal gradients, when the assumption that the mean-free path is small relative to the temperature scale length breaks down. It limits the maximum flux produced by a temperature gradient to some fraction of the total energy flux of a Maxwellian distribution of electrons (with the given density and temperature) moving at the thermal velocity. Typical values of the flux limiter are less than 10% of this physically motivated maximum.[15] The primary effect of the flux limiter is a reduction in the rate of energy propagation through the shell. This inhibition of the transport of energy impacts the computed bang time, and thus the flux limiter and energy multiplier are not independent in their influence on the simulated results. Indeed, at low flux limiter values, higher coronal temperatures and less efficient energy transport into the capsule lead to greater radiation loss, such that a greater absorbed energy is required to achieve a given implosion timing. Their values are therefore generally determined in concert (see, e.g., Ref. 15).

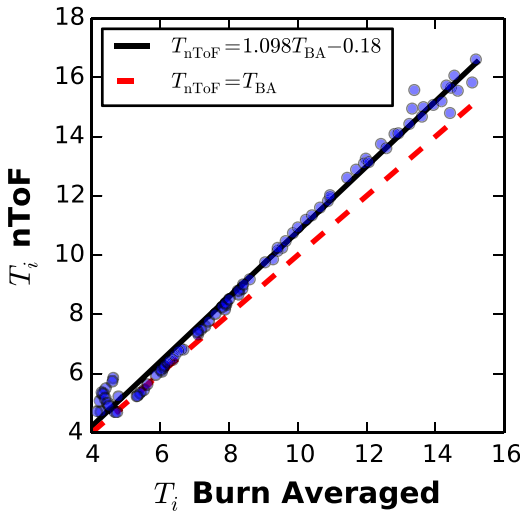

FIG. 5. (Data points) Predictions from an ensemble of 1D Nym simulations of the burn-averaged and synthetic nToF-deduced ion temperatures. The data are well described by a linear relationship $T_{nToF} = 1.098 T_{burn\ average} - 0.18$ (black line). (Dashed red line) Equal temperatures.

The final parameter, a multiplier on the rate of diffusion due to concentration gradients, is used to enhance or reduce the amount of shell material that permeates into the gas. The presence of shell material in the D_2 gas primarily reduces the neutron yield and the neutron-averaged ion temperature. The multiplier scales a diffusion coefficient that models a binary system of ions interacting via screened Coulomb potentials amidst a neutralizing background of electrons [see Eq. (A7)]. To calculate a binary diffusion coefficient, we combine the light species (hydrogen and helium isotopes) into a single component and the heavier species (predominantly carbon and oxygen) into a second component. Limitations of this diffusion model include the binary approximation and the absence of thermo- and barodiffusion, which can be important in ICF systems.[43,44] For additional details of the diffusion model, see Appendix.

We emphasize that the model parameters we determined here are expected to be viable for predicting the scalar performance metrics (bang time, yield, and ion temperature) for sufficiently similar experiments, but may not capture the behavior of experiments with significant excursions from the shots considered here. We make no assertion that the model here will provide an accurate fit to other data measured in our experiments. We do, however, intend to further test the validity of the 1D model developed here by comparing computed Ar spectra with those measured from our shots in a future publication. This comparison could lend additional insight into physical processes that are relevant to the observed performance of these capsules. In particular, comparison of the electron temperature inferred from the time-dependent Ar K-shell spectroscopy will enable us to determine whether the diffusive mixing assumed here is reasonable. If the mixing is more turbulent in nature, we expect that the spectroscopic signal from the Ar may reflect a higher electron temperature than that predicted from this 1D model with diffusive mix since we find the diffusive mix is very effective at cooling the gas, as discussed below.

The settings for each of the parameter-fitting simulations were the same as the nominal pre-shot calculations, except for the variation of the fit parameters, the inclusion of capsule metrology (see Table I), and a geometry-corrected laser drive calculated using a 2D Ares simulation. In the 1D Ares laser model, all incident laser energy is absorbed by the capsule. To estimate geometric losses, including the blow by of laser energy not pointed at the capsule and refractive bending of laser rays away from the capsule, a geometry-corrected laser drive was calculated using a 2D Ares simulation. In the 2D simulation, the capsule absorbed 413 kJ out of the total incident laser energy, representing a 13% loss of energy due to geometric considerations. We then supplied the geometry-corrected laser drive as the laser source for the 1D simulations, with additional attenuation incurred by the energy multiplier. After establishing a post-shot model, we confirmed that the laser energy absorbed in the 1D post-shot Ares simulation generally agreed with that absorbed in a post-shot 1D Nym simulation using a different laser package.

To systematically determine optimal model parameters, we ran ensembles of simulations using LLNL's UQ

Pipeline.[45,46] The UQ Pipeline streamlines the generation of random samples of input parameters, the monitoring of the completion status of each simulation, and the aggregation of the results across all of the simulations. For this study, we performed Latin hypercube sampling[47] of the model parameters within limits anticipated to encompass the parameters of optimal fit. Although an optimization search may have required fewer total simulations, the ensemble sampling approach enabled the running of all simulations in parallel and bypassed potential convergence issues with optimization algorithms. Additionally, the ensemble approach is more efficient than attempting to fit one parameter at a time given that the parameters do not cause independent variations in the results.

Because Shot 2 was the highest performing, the results of the post-shot modeling are presented for this shot in detail; later, we will summarize the best-fit parameters for all three shots. Figure 6 displays the primary performance metrics for each simulation in the ensemble, which included 432 samples of the input parameters. Because three-dimensional data are difficult to visualize, Fig. 6 shows the projections of the data onto each of the 2D output planes. For reference, the experimental performance is indicated with dashed lines with error bars in dotted lines. The colorbar indicates the distance of a given data point from the measured parameters in RMS standard deviations. At a high level, we are able to find good agreement with all three performance metrics. Indeed, about ten samples in the ensemble agreed with all three performance metrics to within experimental uncertainty.

An interesting observation from Fig. 6 is the strong relationship between the bang time and burn-averaged ion temperature. If all of the input parameters had independent effects on the output parameters, one would expect a 2D projection of a 3D dataset to span a planar region in such a plot. Instead, we find the datapoints concentrated near a 1D curve. Such a reduced dimensionality in the simulated performance indicates redundancy in the effects of the adjustable parameters. This can primarily be attributed to both the energy multiplier and the electron flux limiter influencing the effective drive experienced by the capsule. This trade-off has been investigated in detail in other publications.[15]

The results of the fitting procedure are summarized in Table III, including the values of the optimal parameters for each shot and their respective simulated performance. We were able to successfully match all three shots to within experimental uncertainty (with the exception of the ion temperature for Shot 1 being slightly outside the measured range). The

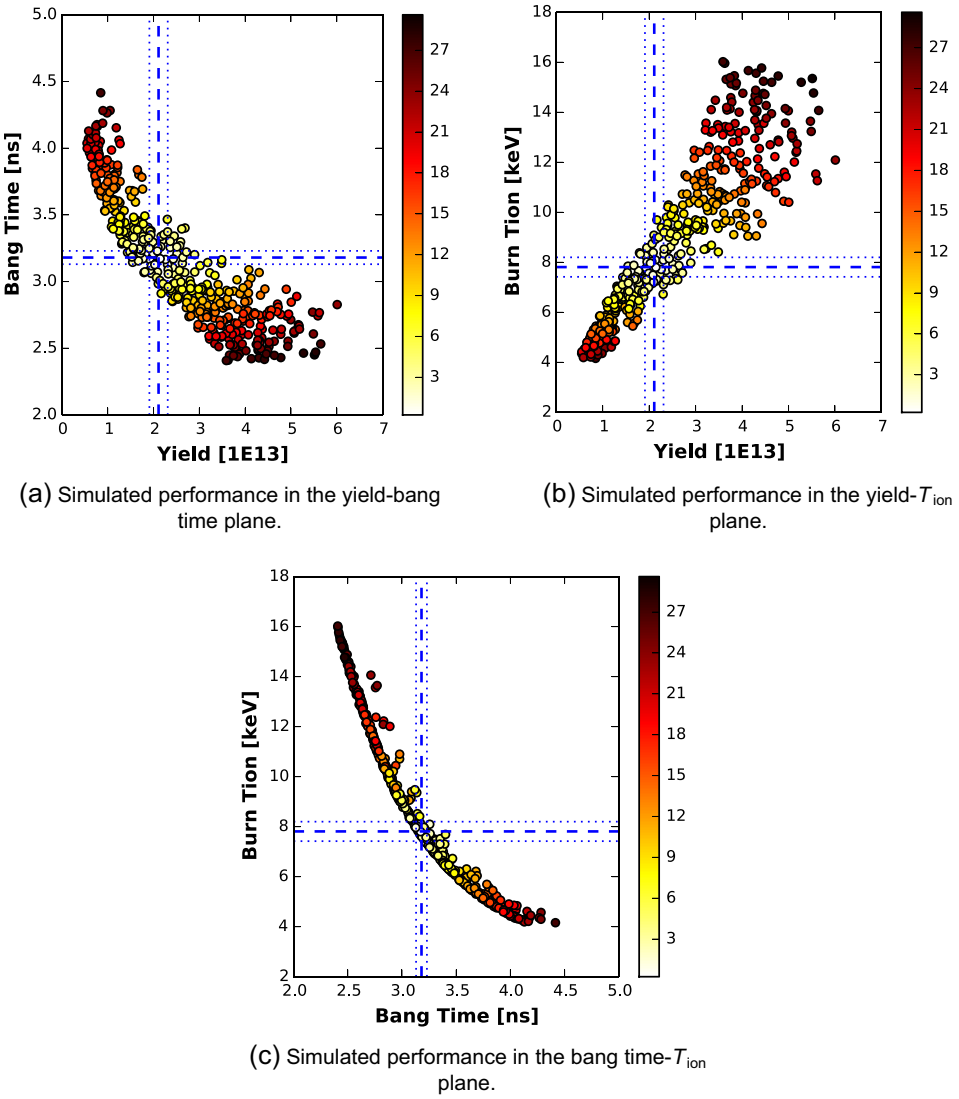

(a) Simulated performance in the yield-bang time plane.

(b) Simulated performance in the yield-T_{ion} plane.

(c) Simulated performance in the bang time-T_{ion} plane.

FIG. 6. Performance of the parameter-fitting simulations, with markers colored by the RMS number of (experimental) standard deviations away from the measured values, i.e., $[\Sigma_i(s_i - m_i)/\sigma_i]^{1/2}$, where s_i is the simulated value of parameter i, m_i is the measured value, and σ_i is the experimental uncertainty.

TABLE III. Summary of model parameters and calculated performance metrics for each of the three shots conducted in the shaping study. The last column indicates the difference between the calculated performance and the actual performance in RMS experimental standard deviations.

	Model parameters			Calculated performance			
Shot	E. Mult.	D. Mult.	Flux Lim.	t_{bang} (ns)	Y_{DDn} (10^{13})	T_{ion} (keV)	σ
Shot 1: N160920-003	0.57	57	0.034	3.26	1.61	7.25	1.1
Shot 2: N160920-005	0.62	50	0.042	3.17	2.14	7.80	0.24
Shot 3: N160921-001	0.58	52	0.069	3.19	1.81	7.52	0.43

best-fit parameters are similar across the three shots: the drive had to be reduced by approximately 40%, while the diffusion was amplified by factors of 50–60. The electron flux limiter exhibits larger variations across the best-fit simulations for the three shots. The variations across the three shots are similar to the variations across the simulations in comparable agreement with a single shot: for simulations that matched Shot 2 to within experimental uncertainty, energy multipliers were typically between 0.6 and 0.65; flux limiters between 0.03 and 0.095; and diffusion multipliers between 45 and 55. This suggests that it may be useful to perform a best-fit determination for matching all three shots simultaneously; however, we chose to fit the shots individually because we could not account for the laser cone fraction variations in the 1D model.

Note that although we varied three input parameters in an attempt to match three output parameters, we were not guaranteed to find simulations that matched the experimental data. For instance, using the one-component-plasma diffusion approximation (see the Appendix), we were only able to match Shot 3 to within experimental uncertainty. Shots 1 and 2 were 2.4 and 1.4 RMS standard deviations away from the data, respectively. We verified that the best-fit parameters were not sensitive to details of the nToF/burn-average ion temperature adjustment; performing a linear fit to only the data between 6 and 8 keV, the same simulations emerged as the best fit to the data.

The particular values of the adjustable parameters have implications for the interpretation of the measured data and the 1D modeling capabilities. Starting with the energy multiplier, the simulations with best agreement truncated the laser energy by approximately 40% relative to the 2D drive, which already accounted for geometric losses of laser energy. This suggests important energy loss mechanisms are missing from the model, such as the laser-plasma interactions believed to be important for the direct-drive configuration.[9] We do not anticipate, however, that laser-plasma interactions would explain the full 40% reduction, but instead interpret this restrictive multiplier as indicative of limitations of the 1D model in accounting for the effects of higher-dimensional hydrodynamic behavior in non-round implosions. It is also possible that the multipliers needed here are compensating for inaccuracies in the physical models assumed for the equation of state and/or transport coefficients of the materials. Recent analyses have demonstrated the impact of these physics models on direct-drive ICF experiments at both NIF and Omega.[48] For the current study, we used LEOS 1014 for D2 and LEOS 5400 for GDP, which are standard models for the equation of state of these materials, described in detail elsewhere.[49–51] We also used a Purgatorio-based model[52,53] for the electronic thermal conductivity of GDP.

Another noteworthy feature of the post-shot model is the significant enhancement of diffusive mixing, with diffusion multipliers typically over 50 for simulations that most closely matched the experimental performance. A large multiplier may be compensating for missing yield-reducing mechanisms, including an unknown combination of multidimensional hydrodynamic effects, errors in the diffusion model (including the neglect of thermo- and baro-diffusion), kinetic effects, preheat, and turbulent mixing. The diffusive mix multiplier serves to increase the amount of diffusion, effectively cooling the hot spot at late times and truncating the neutron production. In Fig. 7, we present the ion temperature history for the post-shot model. In comparison to the pre-shot ion temperature history in Fig. 2(a), the post-shot model reaches similar peak ion temperatures during the initial shock heating, but cools more rapidly due to the presence of diffusively injected shell material in the hot spot.

While the results of our 2D simulations will be reported in detail elsewhere, it is helpful to examine them briefly here in the context of understanding the large multipliers on the diffusion coefficients of our best 1D model. We have observed that diffusion multipliers of around 10–20 are necessary in order to match the measured scalar performance metrics for the three shots in the 2D simulations. The 2D simulations allow for more complex evolution of the fluid dynamics, including deviations from a spherical geometry, so this gives us some indication that a factor of about 2–5 in

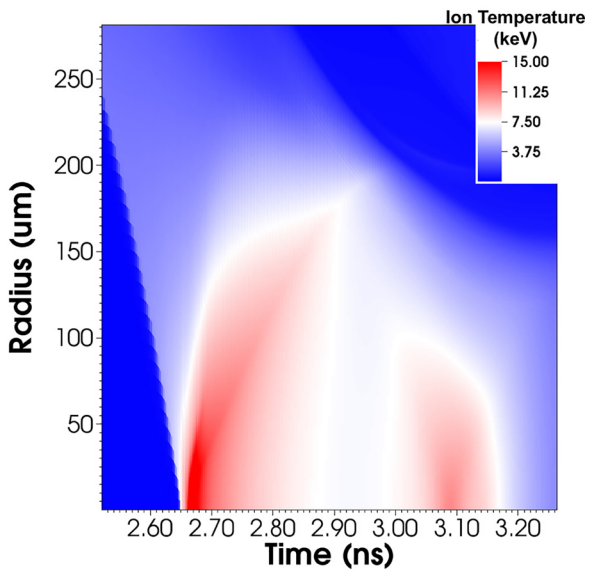

FIG. 7. Ion temperature history predicted by the post-shot model for Shot 2. In comparison with Fig. 2(a), the enhanced diffusive mix cools the hot spot after the initial shock heating.

the 1D diffusion multiplier is needed to compensate for 1D vs. 2D geometry. Another source of yield reduction could be kinetic effects, such as Knudsen-layer depletion.[54,55] We do not believe that the Knudsen effect is a significant source of yield reduction in the current platform because even though the ion mean free path is a large fraction of the gas radius at early time, this does not hold true at the time of peak compression and thermonuclear burn. Although the binary diffusion approximation is a source of error, comparisons with the full, multicomponent solution (including thermo- and barodiffusion) in a similar configuration suggest that the binary diffusion approximation does not greatly underestimate diffusive mixing (see Fig. 9). As mentioned earlier in this section, making a comparison of the spectroscopic data with our simulated electron temperatures should enable us to better ascertain whether the assumption of a diffusion model to reduce the yield is physically reasonable.

During post-shot modeling, we also tested fall-line truncation of the neutron production,[16] which serves as an extreme estimate of 1D hydrodynamic mix penetration. The model truncates neutron production after the shell would have reached $r = 0$ had it maintained its peak velocity. Employing this model, the simulated neutron yields were significantly lower than the measured values for simulations in good agreement with the bang time. The fall-line model over-truncated the burn mechanism, so we resorted to the diffusive mix enhancement.

Upon establishing a tuned, post-shot model, an important (yet difficult to answer) question is: *how predictive is the model?* The employment of the PDXP platform in an additional series of NIF shots performed in Spring 2017 presented an opportunity to test the predictive capability of the post-shot model. In particular, NIF shots N170212-003 and N170212-004 used the same capsule and laser configuration as N160920-005 (Shot 2) with the exception that N170212-004 increased the laser energy by 25%.[18] The gas composition of these experiments differed from those described herein (^{3}He rather than D_2) and the capsules had a larger fill pressure (10.1 atm), but the shots were otherwise identical. The post-shot model for Shot 2 was used to estimate the change in X-ray bang time incurred by scaling the laser energy across these two shots.

The post-shot model proved successful at extrapolating the bang time to a 25% increase in laser energy. The results of the experiment and simulation are shown in Fig. 8, wherein the simulated bang times match the experimental values to within measurement uncertainty. It is desirable to compare against other aspects of the performance to assess the predictive capability of the 1D model. Unfortunately, the D^{3}He yield is confounded by a large uncertainty in the initial D concentration in the 2017 shots, and ion temperatures were not reported in Ref. 18, so further assessment of the model remains for future work.

V. CONCLUSION

A new thin-shelled exploding pusher platform has been fielded at the NIF in the polar-direct-drive configuration. The nominal design employs a 3 mm-diameter capsule with an 18 μm-thick GDP shell filled with 8 atm of D_2 gas and a small amount of Ar dopant. These parameters were chosen to achieve relatively low convergence ratio implosions with sufficiently high temperature to enable time-resolved diagnosis of the temperature histories via spectroscopy. Such time-resolved measurements, positing sufficiently uniform spatial profiles, would provide a valuable additional constraint on integrated simulation tools, potentially enabling validation of collisional heat transport models.

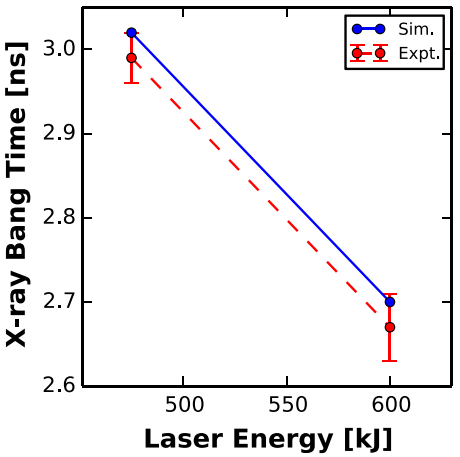

FIG. 8. X-ray bang times (experimental and simulated by the post-shot model) for NIF shots N170212-003 (at 475 kJ laser energy) and N170212-004 (at 600 kJ laser energy), using the PDXP capsule filled with 10 atm of ^{3}He.[18]

As a first step toward developing this platform, three shots conducted in September 2016 varied the laser cone fraction to optimize the symmetry of the polar-direct-drive implosion. Among those shots, N160920-005 achieved the highest performance and roundest implosion. The platform generated 2.11×10^{13} neutrons from DD reactions with a burn-averaged ion temperature of 7.8 keV. Post-shot modeling adjusted 1D simulations to match this performance by reducing the laser drive to 255 kJ (out of the original 475 kJ) and increasing diffusion-induced mix by a factor of 50 to reduce the yield to experimental levels. Such a large enhancement of the diffusion rate suggests that diffusion is not the primary mechanism for yield reduction, but instead points towards multi-dimensional effects. The post-shot model has proven successful at predicting the bang time dependence on laser drive, at least up to a 25% increase. Ongoing work is determining whether the shape of the implosion as a function of laser cone fraction can be correctly modeled in 2D.[24]

Perhaps the most exciting prospects for this platform reside in applications beyond those originally envisioned. The simplicity and diagnostic accessibility of this design have attracted attention from NIF users interested in nucleosynthesis measurements,[18] diagnostic qualification,[19,20] and neutron sources.[21,22] The large capsule size and high ion temperatures are capable of generating significant numbers of thermonuclear reactions. Moreover, the lack of a hohlraum improves diagnostic access and simplifies pre-shot design and target assembly. It is expected that this platform will continue to meet a variety of needs in the high-energy-density community, and that the results presented in this contribution establish a baseline for ongoing modeling efforts.

ACKNOWLEDGMENTS

This work was performed under the auspices of the U.S. Department of Energy by Lawrence Livermore National Laboratory under Contract No. DE-AC52-07NA27344. H. D. Whitley is grateful to the DOE for support provided through a PECASE award. Results from Nym are British Crown Owned Copyright 2018/AWE. The authors are grateful to Lorin Benedict, Paul Bradley, William Cabot, John Hayes, Natalie Krasheninnikova, Robert Managan, Thomas Murphy, Brian Pudliner, and Michael Rosenberg for helpful discussions. LLNL-JRNL-744974.

This document was prepared as an account of work sponsored by an agency of the United States government. Neither the United States government nor Lawrence Livermore National Security, LLC, nor any of their employees makes any warranty, expressed or implied, or assumes any legal liability or responsibility for the accuracy, completeness, or usefulness of any information, apparatus, product, or process disclosed, or represents that its use would not infringe privately owned rights. Reference herein to any specific commercial product, process, or service by trade name, trademark, manufacturer, or otherwise does not necessarily constitute or imply its endorsement, recommendation, or favoring by the United States government or Lawrence Livermore National Security, LLC. The views and opinions of authors expressed herein do not necessarily state or reflect those of the United States government or Lawrence Livermore National Security, LLC, and shall not be used for advertising or product endorsement purposes.

APPENDIX: DIFFUSION MIX MODEL

The physical model used in this work to describe the mixing process of a heterogeneous system is derived from the Boltzmann equation for a coupled system of unique, identifiable particle populations. It is assumed that the mixture is sufficiently collisional to preclude large deviations from the equilibrium, Maxwellian velocity distribution function for each species and is simultaneously sufficiently dilute such that ternary (and higher) collisional events can be neglected. Macroscopic (hydrodynamics-scale) transport equations for the conservation of isotope number density, n_i, mixture momentum, $\rho\vec{u}$, and mixture energy, ρe, are derived using standard techniques from kinetic theory[56,57] and, after some manipulation, can be expressed as

$$\frac{\partial n_i}{\partial t} + \left(\frac{\partial}{\partial \vec{r}} \cdot n_i(\vec{u} + \vec{V}_i)\right) = \dot{w}_i, \tag{A1}$$

$$\frac{\partial \vec{u}}{\partial t} + \left(\vec{u} \cdot \frac{\partial}{\partial \vec{r}} \vec{u}\right) = -\frac{1}{\rho}\left(\frac{\partial}{\partial \vec{r}} \cdot \bar{\bar{P}}\right) + \frac{1}{\rho}\sum_i n_i \vec{X}_i, \tag{A2}$$

$$\frac{\partial}{\partial t}(\rho e) + \left(\frac{\partial}{\partial \vec{r}} \cdot \rho e \vec{u}\right) = -\left(\frac{\partial}{\partial \vec{r}} \cdot \vec{q}\right) - \left(\bar{\bar{P}} : \frac{\partial}{\partial \vec{r}} \vec{u}\right) + \sum_i n_i (\vec{X}_i \cdot \vec{V}_i), \tag{A3}$$

where ρ is the mass density, $\vec{V}_i$, $\bar{\bar{P}}$, and $\vec{q}$, respectively, represent the drift-diffusion velocity, pressure tensor, and heat flux vectors that are driven by atomic-scale collisional processes, while $\dot{w}_i$ and $\vec{X}_i$ express isotopic production/depletion and external forces, respectively. Closures to $\vec{V}_i$, $\bar{\bar{P}}$, and $\vec{q}$ in the global conservation equations above are derived using the Chapman-Enskog approximation,[58] leading to closed-form solutions that depend on the macroscopic state variables and their gradients. Evaluating the drift-diffusion velocities requires consideration of each pairwise interaction between mixture constituents

$$\sum_j \frac{n_i n_j}{n^2 \mathcal{D}_{ij}^{(1)}} (\vec{V}_j - \vec{V}_i) = \vec{d}_i - \frac{\partial \log T}{\partial \vec{r}} \sum_j \frac{n_i n_j}{n^2 \mathcal{D}_{ij}^{(1)}} \left(\frac{D_j^T}{n_j m_j} - \frac{D_i^T}{n_i m_i}\right), \tag{A4}$$

$$\vec{d}_i = \nabla x_i + (x_i - y_i)\nabla(\log P) - \frac{y_i}{P}\left[\frac{\rho}{m_i}\vec{X}_i - \sum_j n \vec{X}_j\right], \tag{A5}$$

where n is the total number density, P is a scalar pressure, T is the temperature, x_i is the atom fraction of the i-th species, y_i is the mass fraction of the i-th species, m_i is the isotopic mass, $\mathcal{D}_{ij}^{(1)}$ is the first-approximation (in reference to the number of terms used in the Sonine polynomial expansion of the Chapman-Enskog method) to the binary diffusivity, and D_i^T is the thermal diffusion coefficient. Here we have assumed electron and ion thermal equilibrium; extensions of this theory to incorporate multi-temperature effects are

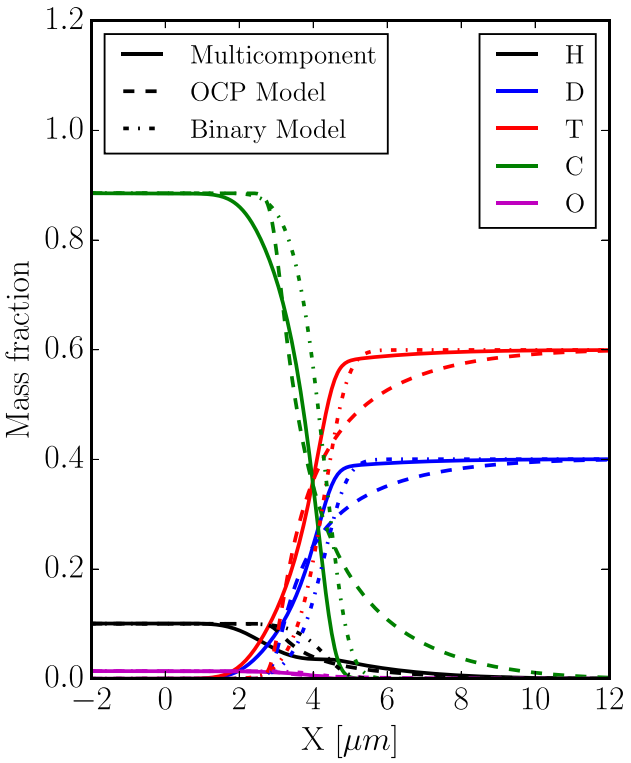

FIG. 9. A comparison of approximate diffusion models against the multicomponent solution for a plastic/deuterium-tritium interface initialized at 0.8 keV and 1.0 keV, respectively. The position X represents a Cartesian coordinate. Initial concentrations were $n_H = 6.305 \times 10^{22}$, $n_C = 4.663 \times 10^{22}$, $n_O = 5.511 \times 10^{20}\,\mathrm{cm}^{-3}$ in the plastic and $n_D = n_T = 2.994 \times 10^{22}\,\mathrm{cm}^{-3}$ in the DT. The profiles are extracted at 30 ps.

available in the literature.[59,60] Following standard procedure in kinetic theory literature,[56,57] the transport coefficients are expressed in a general way using $\Omega_{i,j}^{(l,m)}$ collision integrals that encapsulate the relationship between deflection angle, impact parameter, and particle velocities for a binary collisional event. In this work, the interaction kernel is chosen to be a screened Coulomb potential,[61,62] representing the interactions of ions amidst a neutralizing background of electrons. We use the collision integrals parameterized in Ref. 61.

Equation (A4) represents the inter-diffusion of species i into all other mixture constituents, j. For binary mixtures in the absence of external forces, $\vec{X}_i$, the linear system reduces to

$$n_i m_i \vec{V}_i = -\rho \mathcal{D}_{ij} \left(\nabla y_i + \frac{y_i y_j}{x_i x_j} \left[\frac{(x_i - y_i)}{P} \nabla P + \frac{k_i}{T} \nabla T \right] \right), \tag{A6}$$

where the superscript (1) notation denoting the approximation level of the transport coefficient has been dropped for brevity. If large pressure and thermal gradients are absent, those terms in the diffusion flux may be neglected and the diffusion flux is further simplified to Fick's law

$$n_i m_i \vec{V}_i = -\rho \mathcal{D}_{ij} \nabla y_i; \tag{A7}$$

note $\mathcal{D}_{ij} = \mathcal{D}_{ji}$.

One approximation used in large, multi-physics simulations employs Eq. (A7) in a multi-component environment. Of course, any use of Eq. (A7) in place of the full multicomponent solution will introduce errors in the time evolution of the isotopic compositions; however, this simplification alleviates the computational expense demanded by the dense matrix inversion required for the multicomponent solution [i.e., Eq. (A4)]. Several modeling choices exist for representing the multicomponent system as "binary." At the crudest

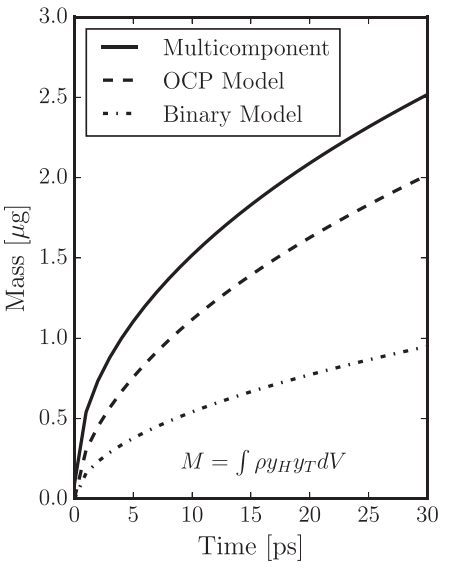

(a) Hydrogen-tritium intermixing.

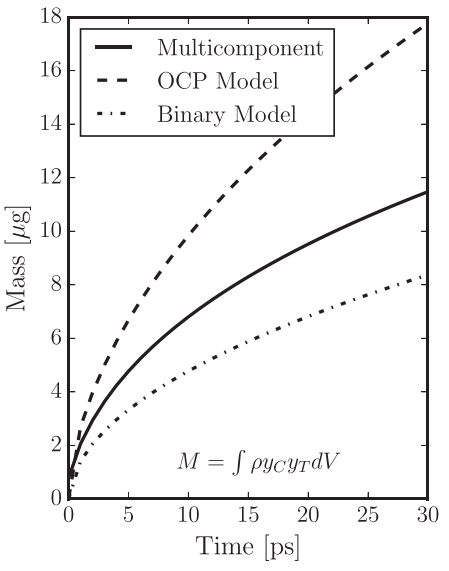

(b) Carbon-tritium intermixing.

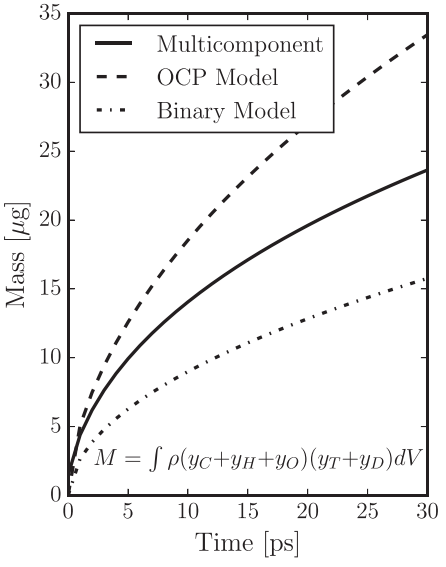

(c) DT-plastic global intermixing.

FIG. 10. Mixing-layer time-histories for several constituent pairs. The simplified "binary" and "OCP" models do not accurately capture the mixing layer structure, evidenced by the penetration of hydrogen and carbon into tritium, as shown in (a) and (b). Global mixing across the interface, shown in (c) indicates the OCP model over-predicts mix, while the binary model under-predicts the mixing process as compared to the rigorous, multicomponent model for this problem.

level of approximation, one can calculate $\mathcal{D}_{ij}$ according to zonally averaged masses and charges, in effect assuming a one-component plasma (OCP). Each species present in the zone then diffuses according to Eq. (A7) with the OCP diffusion coefficient. Alternatively, one can group species into two categories and use average masses and charge states for those two categories to calculate $\mathcal{D}_{ij}$. In the PDXP modeling presented in this work, we use such a binary decomposition with one collection including the light, gas atoms (D, H, T, ^{3}He, ^{4}He) and the other the heavy shell material (C, O). In the shell region, hydrogen was treated as part of the shell material.

The impacts of these simplifications vary from problem to problem and are most significant in situations where the details of the mixing layer structure have a strong impact on the experimental observables. Figure 9 shows a 1.0 keV equimolar deuterium-tritium ($n_D = n_T = 2.994 \times 10^{22}\,\mathrm{cm}^{-3}$) mixture and a 0.8 keV plastic ($n_H = 6.305 \times 10^{22}$, $n_C = 4.663 \times 10^{22}$, $n_O = 5.511 \times 10^{20}\,\mathrm{cm}^{-3}$) mixing interface at 30 ps, evaluated using a variety of diffusion models. These initial conditions set up strong concentration, pressure, and temperature gradients, activating all terms in the diffusion flux. Solid lines in the figure correspond to the solution of the rigorous multi-component model of Eq. (A4), while the binary and OCP models employ Fick's Law, Eq. (A7), with hydrogenic isotopes and carbon/oxygen grouped into a binary approximation, and with the "one-component plasma" approximation discussed previously. This snapshot, taken at 30 ps, reveals the structural differences in the mixing layer predicted by the different models. Closer examination of the mixing layer growth, shown in Fig. 10, reveals that the simpler models fail to capture hydrogen jetting across the material interface that is predicted using the more sophisticated, multicomponent model. Overall mixing layer growth is either under- or over-predicted as compared to the multicomponent model depending on the simplified model employed. Applying scale factors to the simplified models enables an approximate matching of the overall mixing layer growth, but will inevitably fail to capture the detailed structure of the layer.

[1]G. H. Miller, E. I. Moses, and C. R. Wuest, Opt. Eng. **43**, 2841 (2004).
[2]J. Nuckolls, L. Wood, A. Thiessen, and G. Zimmerman, Nature **239**, 139 (1972).
[3]S. W. Haan, J. D. Lindl, D. A. Callahan, D. S. Clark, J. D. Salmonson, B. A. Hammel, L. J. Atherton, R. C. Cook, M. J. Edwards, S. Glenzer, A. V. Hamza, S. P. Hatchett, M. C. Herrmann, D. E. Hinkel, D. D. Ho, H. Huang, O. S. Jones, J. Kline, G. Kyrala, O. L. Landen, B. J. MacGowan, M. M. Marinak, D. D. Meyerhofer, J. L. Milovich, K. A. Moreno, E. I. Moses, D. H. Munro, A. Nikroo, R. E. Olson, K. Peterson, S. M. Pollaine, J. E. Ralph, H. F. Robey, B. K. Spears, P. T. Springer, L. J. Suter, C. A. Thomas, R. P. Town, R. Vesey, S. V. Weber, H. L. Wilkens, and D. C. Wilson, Phys. Plasmas **18**, 051001 (2011).
[4]A. M. Cok, R. S. Craxton, and P. W. McKenty, Phys. Plasmas **15**, 082705 (2008).
[5]S. Skupsky, J. A. Marozas, R. S. Craxton, R. Betti, T. J. B. Collins, J. A. Delettrez, V. N. Goncharov, P. W. McKenty, P. B. Radha, T. R. Boehly, J. P. Knauer, F. J. Marshall, D. R. Harding, J. D. Kilkenny, D. D. Meyerhofer, T. C. Sangster, and R. L. McCrory, Phys. Plasmas **11**, 2763 (2004).
[6]J. A. Marozas, F. J. Marshall, R. S. Craxton, I. V. Igumenshchev, S. Skupsky, M. J. Bonino, T. J. B. Collins, R. Epstein, V. Y. Glebov, D. Jacobs-Perkins, J. P. Knauer, R. L. McCrory, P. W. McKenty, D. D. Meyerhofer, S. G. Noyes, P. B. Radha, T. C. Sangster, W. Seka, and V. A. Smalyuk, Phys. Plasmas **13**, 056311 (2006).
[7]M. J. Schmitt, P. A. Bradley, J. A. Cobble, J. R. Fincke, P. Hakel, S. C. Hsu, N. S. Krasheninnikova, G. A. Kyrala, G. R. Magelssen, D. S. Montgomery *et al.*, Phys. Plasmas **20**, 056310 (2013).
[8]M. J. Rosenberg, A. B. Zylstra, F. H. Séguin, H. G. Rinderknecht, J. A. Frenje, M. G. Johnson, H. Sio, C. J. Waugh, N. Sinenian, C. K. Li, R. D. Petrasso, P. W. McKenty, M. Hohenberger, P. B. Radha, J. A. Delettrez, V. Y. Glebov, R. Betti, V. N. Goncharov, J. P. Knauer, T. C. Sangster, S. LePape, A. J. Mackinnon, J. Pino, J. M. McNaney, J. R. Rygg, P. A. Amendt, C. Bellei, L. R. Benedetti, L. B. Hopkins, R. M. Bionta, D. T. Casey, L. Divol, M. J. Edwards, S. Glenn, S. H. Glenzer, D. G. Hicks, J. R. Kimbrough, O. L. Landen, J. D. Lindl, T. Ma, A. MacPhee, N. B. Meezan, J. D. Moody, M. J. Moran, H.-S. Park, B. A. Remington, H. Robey, M. D. Rosen, S. C. Wilks, R. A. Zacharias, H. W. Herrmann, N. M. Hoffman, G. A. Kyrala, R. J. Leeper, R. E. Olson, J. D. Kilkenny, and A. Nikroo, Phys. Plasmas **21**, 122712 (2014).
[9]M. Hohenberger, P. B. Radha, J. F. Myatt, S. LePape, J. A. Marozas, F. J. Marshall, D. T. Michel, S. P. Regan, W. Seka, A. Shvydky, T. C. Sangster, J. W. Bates, R. Betti, T. R. Boehly, M. J. Bonino, D. T. Casey, T. J. B. Collins, R. S. Craxton, J. A. Delettrez, D. H. Edgell, R. Epstein, G. Fiksel, P. Fitzsimmons, J. A. Frenje, D. H. Froula, V. N. Goncharov, D. R. Harding, D. H. Kalantar, M. Karasik, T. J. Kessler, J. D. Kilkenny, J. P. Knauer, C. Kurz, M. Lafon, K. N. LaFortune, B. J. MacGowan, A. J. Mackinnon, A. G. MacPhee, R. L. McCrory, P. W. McKenty, J. F. Meeker, D. D. Meyerhofer, S. R. Nagel, A. Nikroo, S. Obenschain, R. D. Petrasso, J. E. Ralph, H. G. Rinderknecht, M. J. Rosenberg, A. J. Schmitt, R. J. Wallace, J. Weaver, C. Widmayer, S. Skupsky, A. A. Solodov, C. Stoeckl, B. Yaakobi, and J. D. Zuegel, Phys. Plasmas **22**, 056308 (2015).
[10]T. J. Murphy, N. S. Krasheninnikova, G. Kyrala, P. A. Bradley, J. A. Baumgaertel, J. Cobble, P. Hakel, S. C. Hsu, J. L. Kline, D. Montgomery *et al.*, Phys. Plasmas **22**, 092707 (2015).
[11]P. B. Radha, M. Hohenberger, D. H. Edgell, J. A. Marozas, F. J. Marshall, D. T. Michel, M. J. Rosenberg, W. Seka, A. Shvydky, T. R. Boehly, T. J. B. Collins, E. M. Campbell, R. S. Craxton, J. A. Delettrez, S. N. Dixit, J. A. Frenje, D. H. Froula, V. N. Goncharov, S. X. Hu, J. P. Knauer, R. L. McCrory, P. W. McKenty, D. D. Meyerhofer, J. Moody, J. F. Myatt, R. D. Petrasso, S. P. Regan, T. C. Sangster, H. Sio, S. Skupsky, and A. Zylstra, Phys. Plasmas **23**, 056305 (2016).
[12]Y. P. Opachich, R. F. Heeter, M. A. Barrios, E. M. Garcia, R. S. Craxton, J. A. King, D. A. Liedahl, P. W. McKenty, M. B. Schneider, M. J. May, R. Zhang, P. W. Ross, J. L. Kline, A. S. Moore, J. L. Weaver, K. A. Flippo, and T. S. Perry, Phys. Plasmas **24**, 063301 (2017).
[13]M. D. Rosen and J. H. Nuckolls, Phys. Fluids **22**, 1393 (1979).
[14]A. R. Miles, H.-K. Chung, R. Heeter, W. Hsing, J. A. Koch, H.-S. Park, H. F. Robey, H. A. Scott, R. Tommasini, J. Frenje, C. K. Li, R. Petrasso, V. Glebov, and R. W. Lee, Phys. Plasmas **19**, 072702 (2012).
[15]E. S. Dodd, J. F. Benage, G. A. Kyrala, D. C. Wilson, F. J. Wysocki, W. Seka, V. Y. Glebov, C. Stoeckl, and J. A. Frenje, Phys. Plasmas **19**, 042703 (2012).
[16]S. Le Pape, L. Divol, L. Berzak Hopkins, A. Mackinnon, N. B. Meezan, D. Casey, J. Frenje, H. Herrmann, J. McNaney, T. Ma, K. Widmann, A. Pak, G. Grimm, J. Knauer, R. Petrasso, A. Zylstra, H. Rinderknecht, M. Rosenberg, M. Gatu-Johnson, and J. D. Kilkenny, Phys. Rev. Lett. **112**, 225002 (2014).
[17]L. X. Benedict, M. P. Surh, J. I. Castor, S. A. Khairallah, H. D. Whitley, D. F. Richards, J. N. Glosli, M. S. Murillo, C. R. Scullard, P. E. Grabowski, D. Michta, and F. R. Graziani, Phys. Rev. E **86**, 046406 (2012).
[18]M. Gatu Johnson, D. T. Casey, M. Hohenberger, A. B. Zylstra, A. Bacher, C. R. Brune, R. M. Bionta, R. S. Craxton, C. L. Ellison, M. Farrell, J. A. Frenje, W. Garbett, E. M. Garcia, G. P. Grim, E. Hartouni, R. Hatarik, H. W. Herrmann, M. Hohensee, D. M. Holunga, M. Hoppe, M. Jackson, N. Kabadi, S. F. Khan, J. D. Kilkenny, T. R. Kohut, B. Lahmann, H. P. Le, C. K. Li, L. Masse, P. W. McKenty, D. P. McNabb, A. Nikroo, T. G. Parham, C. E. Parker, R. D. Petrasso, J. Pino, B. Remington, H. G. Rinderknecht, M. J. Rosenberg, J. Sanchez, D. B. Sayre, M. E. Schoff, C. M. Shuldberg, F. H. Séguin, H. Sio, Z. B. Walters, and H. D. Whitley, "Optimization of a high-yield, low-areal density fusion product source at the national ignition facility with applications in nucleosynthesis experiments," Phys. Plasmas (to be published).
[19]B. Kraus, L. Gao, K. W. Hill, M. Bitter, P. Efthimion, M. B. Schneider, H. Chen, J. Ayers, D. Liedahl, A. G. MacPhee, H. Whitley, C. L. Ellison, H. P. Le, R. Bettencourt, R. Kauffman, and D. Nelson, "High-resolution

X-ray spectroscopy of a polar direct drive exploding pusher on NIF," (unpublished).
[20]L. Gao, B. F. Kraus, K. W. Hill, M. Bitter, P. Efthimion, M. B. Schneider, A. G. MacPhee, D. B. Thorn, J. Kilkenny, J. Ayers, R. Kauffman, H. Chen, and D. Nelson, "Absolute calibration of a time-resolved high resolution X-ray spectrometer for the National Ignition Facility (invited)," Rev. Sci. Instrum. (to be published).
[21]C. B. Yeamans, "N170913-001 NIF performance review Sept. 28 2017," Technical Report No. LLNL-PRES-739793, Lawrence Livermore National Laboratory, 2017.
[22]C. B. Yeamans and B. E. Blue, "National Ignition Facility neutron sources," Technical Report No. LLNL-CONF-739397, Lawrence Livermore National Laboratory, 2018.
[23]A. Nikroo, F. H. Elsner, D. G. Czechowicz, J. Gibson, S. E. Grant, A. L. Greenwood, M. L. Hoppe, D. Hysband, B. W. McQuillan, W. J. Miller, J. M. Ponteandolfo, D. A. Steinman, R. B. Stevens, K. R. Schulkz, and M. Takagi, "Capsule production and development for ICF experiments," Technical Report No. GA-A23228, General Atomics, 1999.
[24]Z. B. Walters, H. D. Whitley, C. B. Yeamans, C. R. D. Brown, H. Chen, J. I. Castor, R. S. Craxton, C. L. Ellison, M. Gatu Johnson, W. J. Garbett, E. M. Garcia, F. R. Graziani, G. E. Kemp, C. M. Krauland, B. Lahmann, H. P. Le, K. D. Meaney, P. W. McKenty, J. E. Pino, M. S. Rubery, M. B. Schneider, H. A. Scott, and R. Shepherd, "Post-shot modeling of a polar direct drive platform on the National Ignition Facility," (unpublished).
[25]R. M. Darlington, T. L. McAbee, and G. Rodrigue, Comput. Phys. Commun. **135**, 58 (2001).
[26]B. E. Morgan and J. A. Greenough, Shock Waves **26**, 355 (2016).
[27]P. D. Roberts, S. J. Rose, P. C. Thompson, and R. J. Wright, J. Phys. D: Appl. Phys. **13**, 1957 (1980).
[28]R. C. Malone, R. L. McCrory, and R. L. Morse, Phys. Rev. Lett. **34**, 721 (1975).
[29]S. Atzeni and J. Meyer-ter Vehn, *The Physics of Inertial Fusion: Beam-Plasma Interaction, Hydrodynamics, Hot Dense Matter* (Oxford University Press, 2004).
[30]H. Brysk, Plasma Phys. **16**, 927 (1974).
[31]C. R. Scullard, S. Serna, L. X. Benedict, C. Leland Ellison, and F. R. Graziani, Phys. Rev. E **97**, 013205 (2018).
[32]H. A. Scott, J. Quant. Spectrosc. Radiat. Transfer **71**, 689 (2001).
[33]R. S. Craxton and R. L. McCrory, J. Appl. Phys. **56**, 108 (1984).
[34]S. F. Khan, P. M. Bell, D. K. Bradley, S. R. Burns, J. R. Celeste, L. S. Dauffy, M. J. Eckart, M. A. Gerhard, C. Hagmann, D. I. Headley, J. P. Holder, N. Izumi, M. C. Jones, J. W. Kellogg, H. Y. Khater, J. R. Kimbrough, A. G. Macphee, Y. P. Opachich, N. E. Palmer, R. B. Petre, J. L. Porter, R. T. Shelton, T. L. Thomas, and J. B. Worden, Proc. SPIE **8505**, 850505 (2012).
[35]E. L. Dewald, K. M. Campbell, R. E. Turner, J. P. Holder, O. L. Landen, S. H. Glenzer, R. L. Kauffman, L. J. Suter, M. Landon, M. Rhodes, and D. Lee, Rev. Sci. Instrum. **75**, 3759 (2004).
[36]M. J. May, J. Weaver, K. Widmann, G. E. Kemp, D. Thorn, J. D. Colvin, M. B. Schneider, A. Moore, and B. E. Blue, Rev. Sci. Instrum. **87**, 11E330 (2016).
[37]F. Pérez, G. E. Kemp, S. P. Regan, M. A. Barrios, J. Pino, H. Scott, S. Ayers, H. Chen, J. Emig, J. D. Colvin, M. Bedzyk, M. J. S. I. I. I. A. Agliata, B. Yaakobi, F. J. Marshall, R. A. Hamilton, J. Jaquez, M. Farrell, A. Nikroo, and K. B. Fournier, Rev. Sci. Instrum. **85**, 11D613 (2014).
[38]G. P. Grim, J. P. Finch, N. S. P. King, G. L. Morgan, J. A. Oertel, C. H. Wilde, M. D. Wilke, D. C. Wilson, and D. E. Johnson, Rev. Sci. Instrum. **79**, 10E537 (2008).
[39]J. D. Moody, P. Datte, K. Krauter, E. Bond, P. A. Michel, S. H. Glenzer, L. Divol, C. Niemann, L. Suter, N. Meezan, B. J. MacGowan, R. Hibbard, R. London, J. Kilkenny, R. Wallace, J. L. Kline, K. Knittel, G. Frieders, B. Golick, G. Ross, K. Widmann, J. Jackson, S. Vernon, and T. Clancy, Rev. Sci. Instrum. **81**, 10D921 (2010).
[40]D. E. Bower, T. J. McCarville, S. S. Alvarez, L. E. Ault, M. D. Brown, M. P. Chrisp, C. M. Damian, W. J. DeHope, D. H. Froula, S. H. Glenzer, S. E. Grace, K. Gu, F. R. Holdener, C. K. Huffer, J. H. Kamperschroer, T. M. Kelleher, J. R. Kimbrough, R. Kirkwood, D. W. Kurita, A. P. Lee, F. D. Lee, I. T. Lewis, F. J. Lopez, B. J. MacGowan, M. W. Poole, M. A. Rhodes, M. B. Schneider, N. R. Sewall, F. Y. Shimamoto, S. J. Shiromizu, D. Voloshin, A. L. Warrick, C. R. Wendland, and B. K. Young, Rev. Sci. Instrum. **75**, 4177 (2004).
[41]T. J. Murphy, R. E. Chrien, and K. A. Klare, Rev. Sci. Instrum. **68**, 614 (1997).
[42]B. Appelbe and J. Chittenden, Plasma Phys. Controlled Fusion **53**, 045002 (2011).
[43]G. Kagan and X.-Z. Tang, Phys. Lett. A **378**, 1531 (2014).
[44]A. B. Zylstra, N. M. Hoffman, H. W. Herrmann, M. J. Schmitt, Y. H. Kim, K. Meaney, A. Leatherland, S. Gales, C. Forrest, V. Y. Glebov, M. Schoff, M. Hoppe, and N. Ravelo, Phys. Rev. E **97**, 061201 (2018).
[45]S. Brandon, D. Domyancic, J. Tannahill, D. Lucas, G. Christianson, J. McEnereny, and R. Klein, "Ensemble calculations via the LLNL UQ pipeline: A user's guide," Technical Report No. LLNL-SM-480999, Lawrence Livermore National Laboratory, Livermore, CA, 2011.
[46]J. Tannahill, D. D. Lucas, D. Domyancic, S. Brandon, and R. Klein, in *Proceedings of the 2011 High Performance Computing Networking, Storage and Analysis Conference* (ACM, 2011).
[47]M. D. McKay, R. J. Beckman, and W. J. Conover, Technometrics **21**, 239 (1979).
[48]S. X. Hu, L. A. Collins, T. R. Boehly, Y. H. Ding, P. B. Radha, V. N. Goncharov, V. V. Karasiev, G. W. Collins, S. P. Regan, and E. M. Campbell, Phys. Plasmas **25**, 056306 (2018).
[49]G. I. Kerley, "Equations of state for hydrogen and deuterium," Technical Report No. SAND2003-3613, Sandia National Laboratories, Albuquerque, NM, 2003.
[50]S. Zhang, K. P. Driver, F. Soubiran, and B. Militzer, Phys. Rev. E **96**, 013204 (2017).
[51]S. Zhang, B. Militzer, L. X. Benedict, F. Soubiran, P. A. Sterne, and K. P. Driver, J. Chem. Phys. **148**, 102318 (2018).
[52]B. Wilson, V. Sonnad, P. Sterne, and W. Isaacs, J. Quant. Spectrosc. Radiat. Transfer **99**, 658 (2006).
[53]P. Sterne, S. Hansen, B. Wilson, and W. Isaacs, High Energy Density Phys. **3**, 278 (2007).
[54]K. Molvig, N. M. Hoffman, B. J. Albright, E. M. Nelson, and R. B. Webster, Phys. Rev. Lett. **109**, 095001 (2012).
[55]B. J. Albright, K. Molvig, C.-K. Huang, A. N. Simakov, E. S. Dodd, N. M. Hoffman, G. Kagan, and P. F. Schmit, Phys. Plasmas **20**, 122705 (2013).
[56]J. O. Hirschfelder, C. F. Curtiss, and R. B. Bird, *Molecular Theory of Gases and Liquids* (John Wiley & Sons, Inc., 1954).
[57]J. M. Burgers, *Flow Equations for Composite Gases* (Academic Press, Inc., New York, 1969).
[58]S. Chapman and T. G. Cowling, *The Mathematical Theory of Non-Uniform Gases* (Cambridge Mathematical Library, 1939).
[59]G. Kagan and X.-Z. Tang, Phys. Plasmas **19**, 082709 (2012).
[60]N. M. Hoffman, G. B. Zimmerman, K. Molvig, H. G. Rinderknecht, M. J. Rosenberg, B. J. Albright, A. N. Simakov, H. Sio, A. B. Zylstra, M. G. Johnson, F. H. Séguin, J. A. Frenje, C. K. Li, R. D. Petrasso, D. M. Higdon, G. Srinivasan, V. Y. Glebov, C. Stoeckl, W. Seka, and T. C. Sangster, Phys. Plasmas **22**, 052707 (2015).
[61]C. Paquette, C. Pelletier, G. Fontaine, and G. Michaud, Astrophys. J., Suppl. Ser. **61**, 177 (1986).
[62]L. G. Stanton and M. S. Murillo, Phys. Rev. E **93**, 043203 (2016).